Paper Number: **179**

Title: **An Automated Meshing Framework for Progressive Damage Analysis of Fabrics Using CompDam**

Authors: Andrew C. Bergan

ABSTRACT

A meshing and model construction framework for progressive damage analysis of fabric composites is proposed. A mesoscale idealization is used such that the fiber tows are considered homogeneous and transversely isotropic continua, and the matrix is a homogeneous isotropic continuum. By using this idealization, relatively mature damage modeling techniques developed for laminates of unidirectional plies are transferrable to fabrics. Cohesive interface elements and a continuum damage mechanics (CDM) model implemented in the software CompDam are used to account for the key damage modes including cracking at the tow/matrix interface, transverse matrix cracking in the tows, and fiber breakage in the tows. Matrix degradation is accounted for by plasticity. The modeling approach is demonstrated for a 3D orthogonal woven fabric. The main novelty of the proposed model construction framework is in its flexibility resulting from a formulation that is agnostic to the fabric architecture and implementation using mesh based operations. The algorithm does not make any assumptions about the tow sizes, shape, path, or proximity to other tows, thus it is applicable to a broad range of fabric architectures. The matrix region mesh surrounding the tows is constructed from domain boundary and tow surface meshes (i.e. through a series of mesh-based operations) such that the model domain can be arbitrarily shaped.

INTRODUCTION

There has been a long-standing trend of increasing use of analysis to evaluate different composite materials and structural details for aerospace applications, which both reduces cost and broadens the practical design space. One class of analysis tools that has received significant attention as part of this overall trend is progressive damage analysis (PDA) methods to predict the strength, damage tolerance, and life of composite structures. Recently, significant advances have been made in the development and demonstration of predictive capability of PDA methods, e.g. [1–4]. In particular, under

Andrew Bergan, Durability, Damage Tolerance, and Reliability Branch, NASA Langley Research Center, Mail Stop 188E, Hampton, VA 23681

the NASA advanced composites project (ACP), CompDam, the floating node method, and Rx-FEM have shown great promise for failure modes dominated by delamination and matrix cracking in unidirectional tape laminated structures [5–14]. However, relatively little progress has been made toward PDA methods for composites using fabric architectures. One premise of this paper is that PDA methods developed for unidirectional plies homogenized at the ply-level can be adapted for use in fabrics homogenized at the tow level with few modifications. It is presumed that, in both laminates and fabrics, the relevant length scale is on the order of ~1 mm, referred to as the mesoscale. Each material point includes hundreds of fibers homogenized as an orthotropic or transversely isotropic continuum. Of course, with fabrics, the tow geometry and architecture introduce a critical added level of complexity as compared with traditional laminated composites.

Mesoscale fabric models have been developed by several authors with an aim to balance the accurate representation of fiber content and orientation in the tows, with geometric complexity and the associated model construction effort and robustness. In all fabric models, accurate representation of the fiber content and orientation is the most fundamental consideration (as in traditional laminated composites) and is required to predict stiffness and strength accurately [15]. Recently, it has been suggested that tow shapes must also be accurately represented [16–18]. As a result, many authors have pursued numerical and experimental methods to obtain detailed fabric tow geometric information. On the numerical side, one popular method is the multiple-chain digital element method [19–21], which simulates the manufacturing processing by representing each tow as comprising a set of filaments that may contact and slide while compacted into the final form. The result of the simulation is realistic tow geometries that can account for nesting, fiber content variation, and cross-section variation. Instead of simulating the contact problem, others have used a topological methods for correcting interpenetrations [22]. Researchers have also attempted to use direct measurements of tow geometry obtained from X-Ray computed tomography (CT) to construct models, e.g. [17, 23]. However, at present, no single approach has been demonstrated to be superior for a broad set of fabrics. Obtaining an accurate and robust geometry model for a variety of fabric architectures remains a challenging task.

Creating a mesoscale finite element model from the geometry model is also a challenging task. The geometry model is typically a surface mesh or point cloud and may have features that are inadmissible for finite element analysis, e.g., tow interpenetrations. Computer aided design (CAD) engines have been used to translate the surface geometry model into a solid geometry model valid for conventional meshing algorithms for plain weaves [24] and triaxial braids [25, 26]. The general approach is to loft together spline surfaces fit to the geometry model. Boolean operations are used to remove small slivers occurring between adjacent tows and to create the matrix geometry. However, since boolean operations are not closed under spline representation [27], the CAD engine typically has finite precision, and there are unavoidable errors in the geometry fitting, it is only possible to obtain a valid conformal solid geometry for the tows and matrix for simple architectures. In references [24–26], a fictitious thermal contraction (to remove interpenetrations) and subsequent thermal expansion analysis considering contact is used to obtain a valid conformal solid CAD model of the tows and matrix prior to mesh generation.

For complex fabric architectures, such as 3D orthogonal weaves, most researchers have introduced arbitrary geometry adjustments to facilitate conformal meshing or used

alternative methods that avoid the need to generate a conformal mesh. For example, in a recent analysis of 3D orthogonal weave, the authors enforce a minimum separation between all the tows to avoid meshing difficulty [28]. Voxel meshes have been found to generate good predictions for stiffness, but their ability to account for progressive damage (especially Mode II fracture along tow boundaries where special considerations are needed to prevent interlocking on jagged edges) is not clear, e.g. [29]. Others have introduced specialized methods for preprocessing or as part of the analysis to subdivide elements along tow boundaries within a nonconforming structured hexahedral mesh [30, 31].

In this paper a meshing and model construction framework for mesoscale PDA of fabric composites is proposed. The approach introduces few assumptions on the input and uses surface mesh and solid mesh operations to construct the tow and matrix region meshes (avoiding the complications of CAD representation). Following the approach in [24–26], tows are considered touching when they are within a critical distance. Touching tows are connected with cohesive interface elements. Damage is considered in the tows using the continuum damage mechanics (CDM) code CompDam [32]. The tow/matrix interfaces are also allowed to debond using cohesive elements. In addition, matrix degradation is accounted for by plasticity. The main novelty of the proposed model construction framework is in its flexibility resulting from a formulation that is agnostic to the fabric architecture and implementation using mesh based operations. The algorithm does not make any assumptions about the tow sizes, shape, path, or proximity to other tows, thus it is applicable to a broad range of fabric architectures. The matrix region mesh surrounding the tows is constructed from domain boundary and tow surface meshes (i.e. through a series of mesh-based operations) such that the model domain can be arbitrarily shaped.

This paper is organized as follows. First, a geometry model is generated for a 3D orthogonal weave. The geometry model is compared against X-Ray CT scans of a test specimen to evaluate its accuracy. Then, the geometry model is used to demonstrate the proposed meshing and model construction approach. Finally, a demonstration of the model capability is provided for uniaxial warp-direction tension loading.

GEOMETRY MODEL

A representation of the fabric tow geometry within the model domain is a required input for the current method. The geometry is provided as a series of cross sections for each tow (or, equivalently a surface mesh) and a surface mesh defining the model boundary. This generalized input is advantageous in that it allows for arbitrary non-idealized fabric geometries, which may be obtained from other models, dry-fabric simulations (e.g., multi-chain digital element method), experimental observations (e.g., X-ray computed tomography), or some combination thereof, for any class of fabric. Further, it is noted that the mesoscale model boundary need not be rectilinear.

In the current line of work, the virtual textile morphology suite (VTMS) software [33] has been used to generate the input fabric geometry for a 3D orthogonal weave for which no realistic geometry model existed. The VTMS geometry model is constructed based on several point measurements made from an X-Ray CT scan of the material. The process used to create the tow geometry is described in this section.

Fabric geometry generation

The VTMS software uses the multi-chain digital element method [19–21] to create realistic morphology of fabric tows. In the method, each tow is represented as a collection of rod-element-chains referred to as filaments. When two chains come within a critical distance, contact and friction between the adjacent elements is enforced. Realistic morphology can be obtained after an iterative process of relaxation and compaction. During these steps, the filaments move with respect to each other producing varying cross sections along the length of the tow. Relaxation is simulated by applying tensile force in the filaments, calculating the forces at each node considering contact, and then solving the governing equations to find a minimum energy equilibrium state. Compaction can be applied by translation and relaxation or by contact with simulated tooling. In both cases, the filaments are moved such that the thickness of the model reduces and the number of contacts and/or interpenetrations increases. Compaction and relaxation are applied iteratively until the desired thickness is obtained. By iteratively applying compaction and relaxation, the fabric manufacturing process can be approximated.

A VTMS model was constructed of the particular 3D orthogonal weave studied herein. Images of the model at several stages in the simulation process are shown in Figure 1. The model was based on measurements and observations from an X-Ray CT scan of a 1 inch-square sample cut from a 0.125 inch-thick flat plate; 'SN005' in reference [34]. The key parameters used to setup the model are as follows. The warp

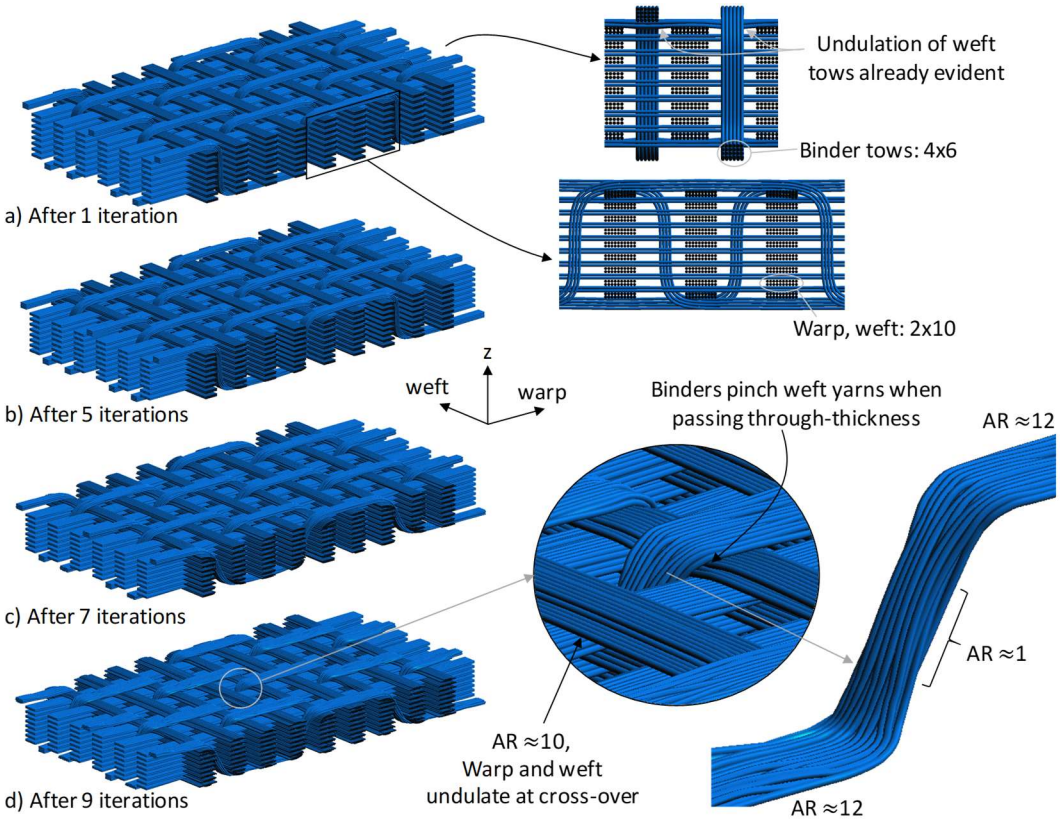

Figure 1. Geometry model generation using the VTMS software.

and weft tow spacing were set to 2.56 mm and 2.88 mm. The material has 8 layers of warp tows and one binder tow per dent (space between the warp tow stacks) with the binder pattern shown in Figure 1. The tow filament arrangements and diameter is selected as follows. The choice of filament diameter is driven by the trade-off between accuracy and computational cost. Increasing the number of filaments improves the fidelity and accuracy of the tow geometry [20, 21]. However, additional filaments increase the computational time exponentially since the not only do the number of filaments increase, but at the same time the element length must be decreased for solution stability. Previous work suggests about 20 filaments per tow is a good trade-off [21]. Since the binder tows have a thickness-to-width aspect ratio (AR) near one where they traverse the thickness, whereas the warp and weft tows have a much higher AR (~12), filament patterns roughly corresponding to the measured tow ARs were specified; 4x6 for the binder tows and 2x10 for the warp and weft tows. Considering these filament arrangements, the filament diameter of 0.1144 mm was selected for agreement with measurements of tow thickness and width in several locations using a least squares minimization.

The series of snapshots shown in Figure 1a-d highlight how the simulation process represents the manufacturing compaction eventually arriving at tows with undulating paths and variable cross sections reminiscent of the actual material. Some details of the final geometry obtained from the simulation are shown in the lower right corner of the figure. The aspect ratio and cross-section shape of the binder tows changes dramatically as they transition from the surfaces to traversing the thickness of the plate. At all locations where tows crossover each other, they are in contact, as occurs in the actual dry preform.

Each deformed filament-based tow is homogenized in order to generate a tow-level mesoscale geometric representation. The filament-based tows are homogenized as described in reference [21], summarized briefly as follows. At several locations along the tow, the tow perimeter is defined as the contact points between the filament tows and a virtual dial that is rolled around the circumference of the tow. The result is a series of profiles that define the tow surface, which are converted to a surface mesh representation. The process is repeated for each tow independently. The resulting

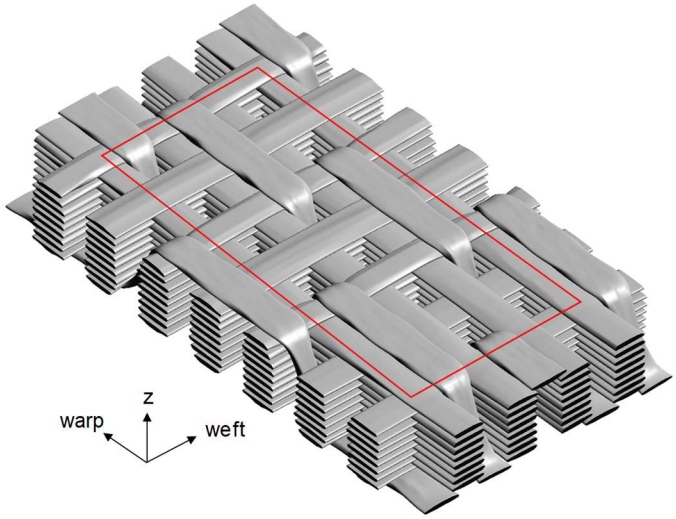

Figure 2. Tow surface geometry after homogenization step.

surface mesh is show in Figure 2. The surface mesh is cropped to one repeating unit cell (RUC) yielding 98 tows, as shown by the red box in Figure 2.

The size of the model domain is selected as one RUC here since it is the smallest representative domain and therefore provides the simplest and most computationally efficient means to demonstrate the proposed methods. For the purpose of predicting damage progression in structural elements, the issues of length scale separation and localization of damage prohibit utilization of RUCs with periodic boundary conditions [35]. Therefore, the intended future applications will typically require larger domains containing multiple RUCs embedded within a global structural model, e.g. [36]. A multiple RUC geometric model can be obtained by tessellating the current RUC geometry.

As a result of approximating the filament-base tows as a homogenized surface and conducting this operation on individual tows, the resulting tow surfaces inevitably have interpenetrations. Both VTMS and the proposed tool have the ability to remove interpenetrations by identifying interpenetrating nodes and moving them toward the interior of the tow iteratively until the interpenetration is removed. Since most analysis methods require matrix between all of the tows, an additional compensation is often employed during the penetration removal process so that a user-defined gap is inserted between the tows, e.g. [29, 28]. Since one of the paradigms of the current approach is direct consideration for "touching" tows, no extra compensation is needed.

The overall representativeness of the model can be evaluated by comparing the fiber volume fraction with test measurement. The fiber volume fraction measured by acid digestion was reported as 47.4% [34]. Assuming the fiber volume fraction within the tows is 80% (other authors have made the same assumption, e.g. [17, 37]), the overall fiber volume fraction in the model is 46.1%. It is noted that this is a substantial improvement compared with the 50.9% fiber volume fraction predicted by a model with an idealized unit cell, which used nonphysical binder tow geometry [34].

Comparison with X-Ray CT data

A qualitative comparison of the VTMS-generated geometry and the X-Ray CT data for a few slices normal to the nominal warp, weft, and z directions is instructive for

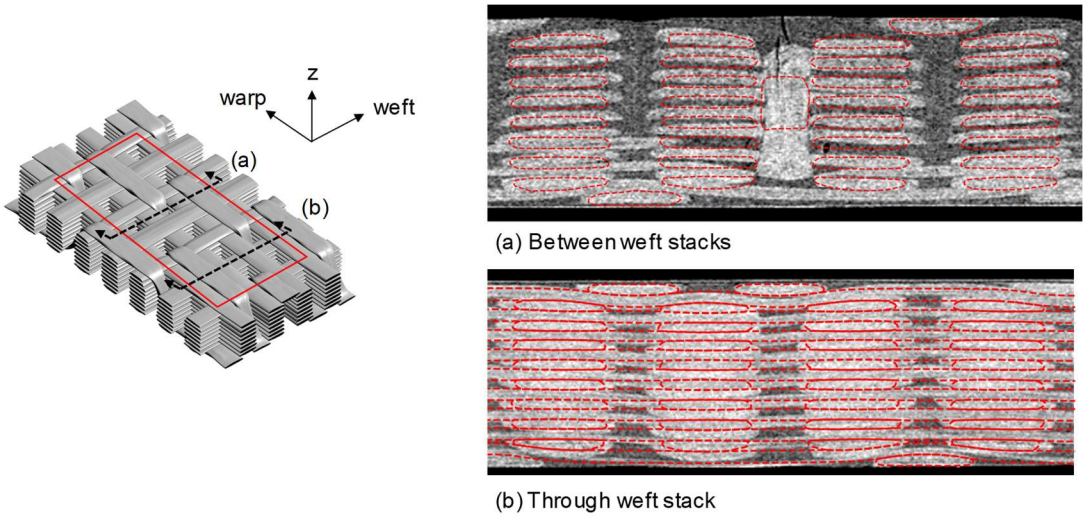

Figure 3. Overlay of geometry model and X-Ray CT for two slices normal to the warp direction.

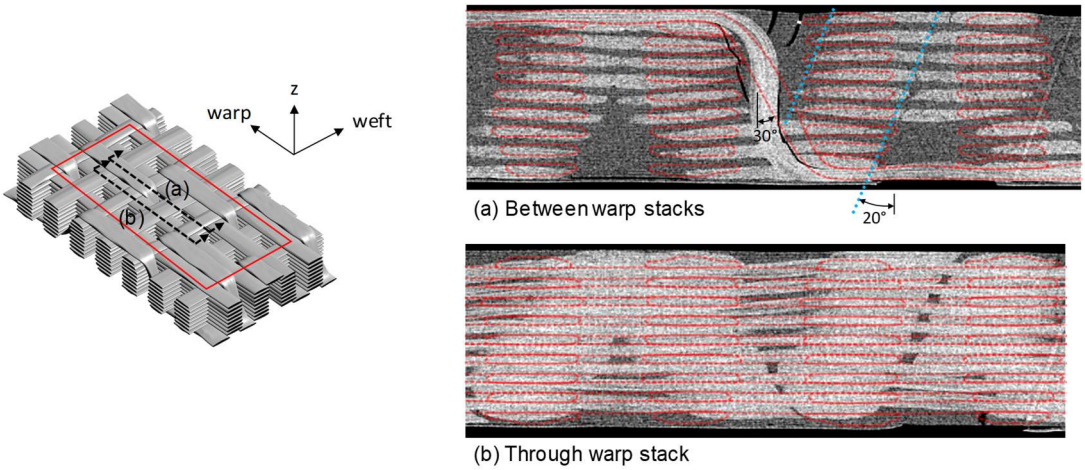

Figure 4. Overlay of geometry model and X-Ray CT for two slices normal to the weft direction

evaluation of the geometric model's accuracy. The two data sources are overlaid on the selected slices. Two representative slices normal to the nominal warp direction are shown in Figure 3. A slice nominally between two weft stacks is shown in Figure 3a and a slice nominally through the center of a weft stack is shown in Figure 3b. In both cases, the overall agreement between the model (red dashed lines) and the X-Ray CT scan is very good. In general, the tow locations, sizes, and aspect ratios are similar. The binder-tow-induced waviness in the warp and weft tows is in good agreement. In general, the warp and weft tows and the portions of the binder tows at the top and bottom surfaces of the plate, have a slightly lower aspect ratio in the model than in the actual specimen. In Figure 3a, the most apparent discrepancy between the model and the scanned specimen is in the binder tow. In the mode, the binder tow is inclined as it traverses through the plate thickness whereas it is nearly vertical in the scan (this observation is clearer in Figure 4). A minor discrepancy is the spacing in the z-direction between internal warp tows. This spacing is irregular in the test specimen and is a variability that is not captured in the model.

Two representative slices normal to the nominal weft direction are shown in Figure 4. A slice nominally between two warp stacks is shown in Figure 4a and a slice nominally through the center of a warp stack is shown in Figure 4b. In contrast to Figure 3, these comparisons show more limited agreement between the model and the scan. Considering Figure 4a, the portions of the binder tows along the top and bottom surfaces of the plate, and the weft tow size and aspect ratio are in relatively good agreement.

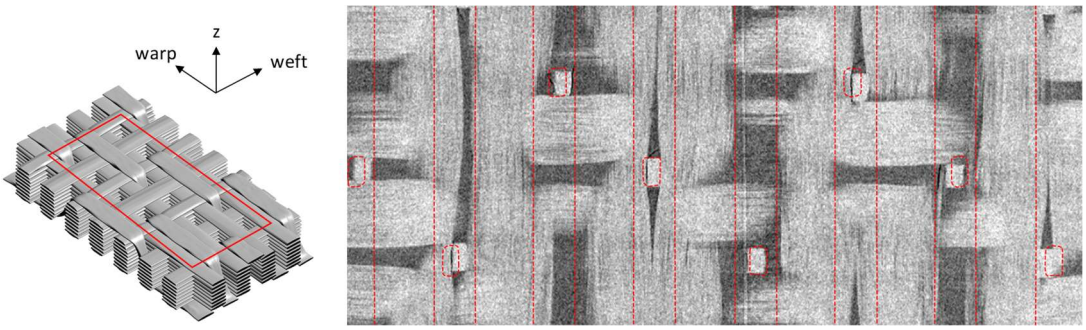

Figure 5. Overlay of geometry model and X-Ray CT for a slice normal to the z-direction at the plate midplane.

The weft tow locations differ substantially between the model and the scan. The weft tow stacks are inclined at an angle of about 20° in the as-manufactured specimen, as is highlighted with the blue dotted lines in the figure. This inclination was not introduced into the geometry model, so the weft stacks in the model are aligned vertically. Additionally, where the binder tow traverse the thickness, it is approximately vertical (in the z-direction) at the midplane of the plate as can be observed in the scan shown in Figure 4a. In the model, the binder appears to be too "tight" traversing the thickness of the plate at about 30° from vertical. The VTMS software is capable of producing a model that reduces these discrepancies between the model and the scan. Additional modeling effort to rectify these differences was outside the scope of the current study. Since the focus of the present paper is on the PDA model construction, the geometry described here was considered adequate for demonstration purposes.

A slice at the midplane of the plate, normal to the z-direction, is shown in Figure 5. The figure shows that the location, size, and aspect ratios of the binder tows are in good agreement between the model and the scan. The slice is taken through the midplane of the weft tows, where it can be seen, as it was shown in Figure 4, that the weft tow spacing in the warp direction is irregular in the scanned specimen.

FINITE ELEMENT MODEL GENERATION FRAMEWORK

A finite element model suitable for PDA is generated from a geometric model as follows. At the highest level, the steps in the process are to model the tows, then the matrix, and finally to assemble the tows and matrix. Each tow and the matrix are meshed separately such that their meshes are not required or expected to match at the interfaces. This approach enables for relatively simple and robust meshing, whether the mesh size is coarse or highly refined. Throughout this section, the 3D woven model described in the previous section is used as an example, aiming for a target element edge length of 0.2 mm. However, the procedures presented make no assumptions about the architecture and relatively few assumptions about tow shapes. Thus, the procedure is directly extendable to different 2D and 3D fabric architectures with an arbitrary level of mesh refinement. The procedures used to generate the model are described in the following subsections.

Tows

Robustly generating a high quality hexahedral mesh suitable compatible with CompDam for arbitrary tows is a challenging problem. In order to have broad applicability, the particular format of the tow geometry input should be as general as possible, while the output mesh should share consistent features required for accurate damage analysis. For compatibility with CompDam, a swept hexahedral mesh with elements aligned with the fiber direction is implemented. Since the fiber volume fraction of the tows is relatively uniform, the cross-sectional area is also relatively consistent along the length of the tow. This, combined with a fiber aligned meshing approach for use of CDM, makes swept meshing a suitable approach. Thus, a swept mesh generation algorithm is developed as described below, and applied separately to each tow. The steps described here are implemented in Python using Trimesh [38] and NumPy [39] and are fully automated.

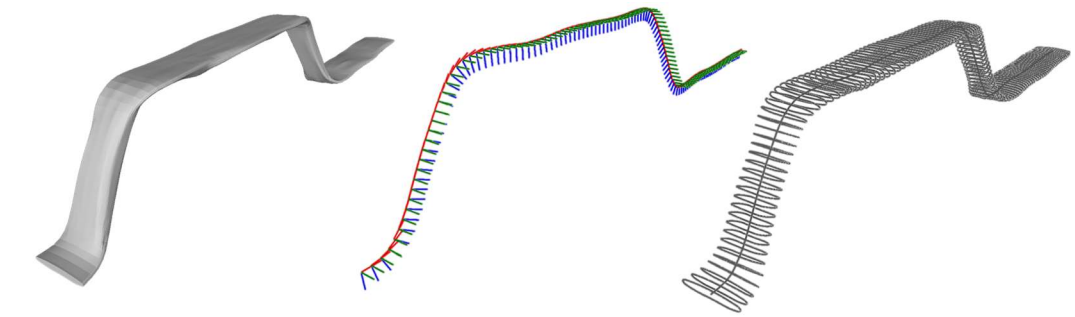

Figure 6. A series of profiles normal to the tow centerline and the material directions for one tow.

While the initial input can be either a triangular surface mesh or a series of cross sections, assume for now that the input is a surface mesh (this assumption is relaxed below). An example binder tow is used to illustrate the procedure; the input surface mesh is shown in Figure 6a. To generate a solid swept mesh, a series of seeded profiles are established along the length of the tow, as follows. The centerline of the tow is identified as the centroids of planar slices taken normal to the major axis of the tow. For the present 3D orthogonal weave, the major axis of the tows are either warp or weft. The centerline is resampled as a set of uniformly spaced points with the number of points determined based on the target element size in the fiber direction. Each of these points along the centerline will be the centroid of the seeded profiles used for mesh generation. Next, the profile normal directions are calculated as the average of the centerline vectors adjacent to the profile centroid point, shown as the red lines in Figure 6b. Then, the surface mesh is sliced using these centerline points and normals, producing the profiles shown in Figure 6c. By principal component analysis, the major axes of each profile is identified (green lines in Figure 6b). The minor axis of each profile is found from the cross product of the normal and major axis. The material coordinate system at each profile location is thus defined with 1-direction being along the profile normal, the 2-direction along the profile major axis, and the 3-direction along the profile minor axis. It is assumed that material coordinates vary only as a function of position along the tow centerline.

The profiles are seeded to facilitate the swept meshing approach as follows. The profile is transformed to its local coordinates system with the major and minor axes the abscissa and ordinate, respectively. The profiles is divided into four segments, one for each quadrant of the local coordinate system. For example, the 50th profile from Figure 6c is shown divided into four segments each with a different color (red, blue, orange, and green) in Figure 7a. Since the profiles are obtained by slicing the triangular surface mesh, they are piecewise linear. The profile vertices are shown as ‘x’ markers in Figure 7a. The profile is resampled in each quadrant with an equal number of uniformly spaced seeds, shown as the purple triangular markers in Figure 7a. The number of seeds is a user-defined parameter that determines the mesh size in the transverse direction. In the example shown Figure 7a, 40 seeds define the perimeter of the profile. The resulting mesh perimeter approximates the original profile well with some deviations in the regions of high curvature on the left and right side of the tow cross section. Finally, the interior of the profile is discretized. The algorithm uses triangular elements near the regions of high curvature and quadrilateral elements elsewhere with two or four elements through the thickness of the tow. The final 2D mesh is shown in Figure 7b

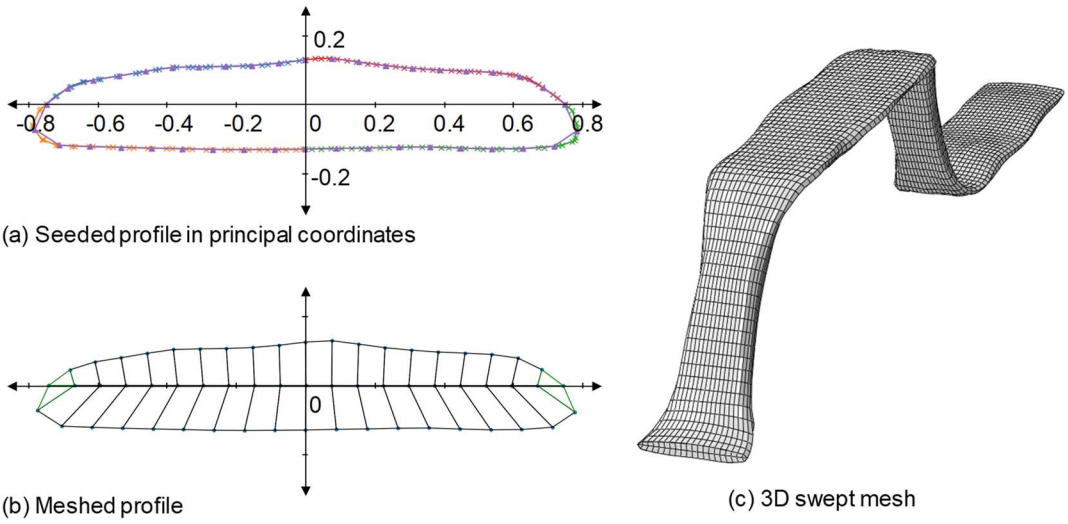

Figure 7. Swept mesh generation. Coordinates are in mm.

where two elements are used through the thickness of the tow. Repeating the process for all profiles, then sweeping together to form a 3D solid mesh, yields the result shown in Figure 7b for this binder tow.

In the case when the input is a series of cross sections, the code generates an initial triangular surface mesh as follows. If all profiles defining the tow have the same number of points, a surface mesh can be generated directly following the algorithm in reference [37]. For profiles defined with varying numbers of points, the resampling algorithm described above (shown in Figure 7a) is used to obtain a set of uniform profiles from which a surface mesh is generated. More sophisticated surface meshing algorithms are available for processing and smoothing point cloud data (e.g., [40]) and could be introduced at this stage if needed. Having a surface mesh, the solid mesh generation algorithm proceeds as described above.

The final mesh contained about 4,000 reduced-integration solid continuum (C3D8R) elements for each warp and binder tow, and about half as many of the same type of elements for each weft tow. The total number of solid continuum elements for the 98 tows is about 257,000.

After generating solid element meshes by applying the series of interpolations described above on all the tows, two additional post-processing steps are needed. First, it is possible that the tow meshes interpenetrate where edges of adjacent tows are both concave (i.e. saddle points). Therefore, interpenetration algorithm is applied again where interpenetrations are removed by iteratively moving the interpenetrated nodes toward the interior of the tow (as described above). Second, the locations where the tows touch is identified as follows. For each tow, nodes within a critical distance of an adjacent tow are identified in a set. The element faces shared by three or more nodes in the set are defined as the surface where the tow touches the adjacent tow. Each tow touches several other tows at the locations where they crossover each other. In the present implementation, warp-weft and binder-weft touching tow pairs are considered, while the relatively small patches where warp and binders tows touch are ignored. After all the tow-touching regions are identified, the remaining tow surface not in contact with another tow is assumed to be in contact with the matrix.

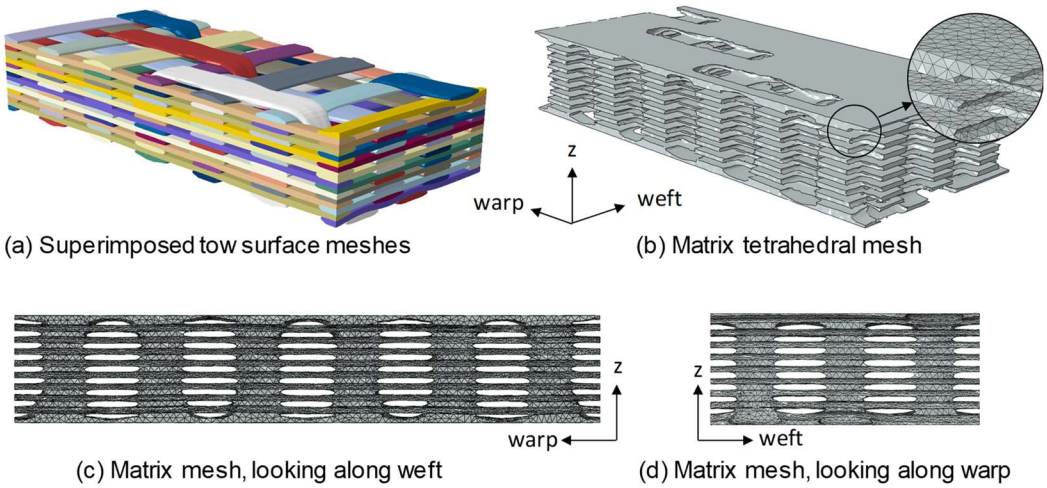

Figure 8. Matrix mesh generated from tow surface meshes.

Matrix

Difficulty in obtaining meshes of the matrix region in mesoscale fabric models has been a major impediment in the past. By allowing the tows to touch, the current approach alleviates one difficulty: narrow slivers of matrix between tows. However, even without matrix slivers between tows, mesh generation for the matrix region remains nontrivial due to the complex geometry of the matrix volume.

The recent development of the tetrahedral meshing algorithm TetWild addresses several of the previous technical barriers in triangulating the interior of arbitrary surface meshes, and has been demonstrated to be very robust [27, 41]. A key insight of the TetWild algorithm pertinent to this work is that deviations in the input surface mesh within a user-defined envelop are ignored. In other words, the algorithm eliminates regions where matrix slivers would ordinarily be created. Further, the input surface mesh does not need to watertight or meet other mesh quality requirements. Thus, the algorithm allows for the tow surface meshes to be used directly to generate the matrix mesh.

The matrix mesh is obtained with two successive meshing operations. All of the tow surface meshes are superimposed (Figure 8a) and a then a slightly larger bounding box is meshed. The TetWild algorithm meshes the full domain containing both the tows and surrounding matrix region. The winding number (see [42]) is used to separate the tow and matrix meshes, retaining the matrix mesh.[1] A mesh boolean operation is used to trim the matrix mesh to the final model domain using PyMesh [43, 44]. The result is remeshed since the boolean operation is a geometric operation that produces element shapes that are not appropriate for finite element analysis. The resulting matrix mesh is shown in Figure 8b-d. The final mesh contains 368,000 quadratic tetrahedral (C3D10) elements. Element-based surfaces are created in the cavities of each tow. It is noted that all of the matrix creation operations can be fully automated. However, at this stage the element-based surface creation and data transfer between codes are manual steps.

[1] The tetrahedral meshed tows can be used if preferred to the proposed hexahedral meshing algorithm. For the purpose of applying CompDam, hexahedral elements are required.

Model assembly

The meshes for the matrix and each tow are loaded into Abaqus/CAE [45] as individual parts and assembled as described in this section. As in the generation of the tow and matrix meshes, the procedure used for assembly is largely automated, making use of the Abaqus/CAE Python API.

The tow/tow and tow/matrix interfaces are likely locations for cracking and so the meshes are connected with cohesive elements and tie constraints at these interfaces, analogous to the fiber aligned meshing approaches used to model traditional unidirectional tape laminates with CompDam [11, 14, 46]. For each tow, cohesive elements are extruded on its surface with near zero thickness. In total, about 244,000 cohesive elements are added to the model. The sets defining the regions where the tow touches adjacent tows and the matrix are transferred to the corresponding cohesive element faces and nodes. Next, tie constraints are added to connect the tows and matrix together, with the slave surface being the cohesive element surface and the master surface being the continuum element surface. The slave nodes to be included in each tie constraint are specified directly (as opposed to using a search algorithm wherein the tied nodes are identified by the solver) as the nodes on the cohesive element surface. An example of the tied surfaces for one tow/matrix tie are shown in Figure 9.

The tie constraints for the tow/tow interface follow the same method as outlined for the tow/matrix interface with an added complexity that the tows both have cohesive elements. An example of the tow/tow interfaces for one binder tow are shown in Figure 10. As noted previously, the ties are established based on nodes within a critical distance to a neighboring tow. The resulting tied surfaces are shown in red in Figure 10a. A 2-D schematic of the cohesive elements and tie constraints at one tow/tow interface is shown in Figure 10b. The cohesive element thickness is exaggerated for illustrative purpose as the gray, orange, and blue colored layers adjacent to the continuum elements. The blue

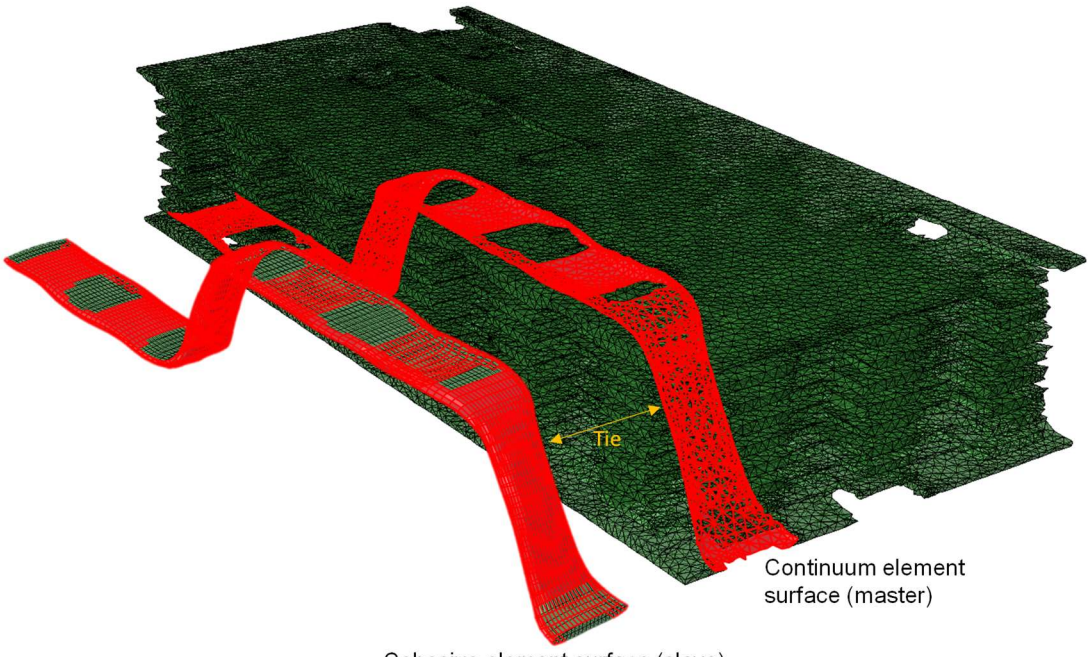

Figure 9. Exploded view of tow/matrix tied surfaces (highlighted in red) for one binder tow.

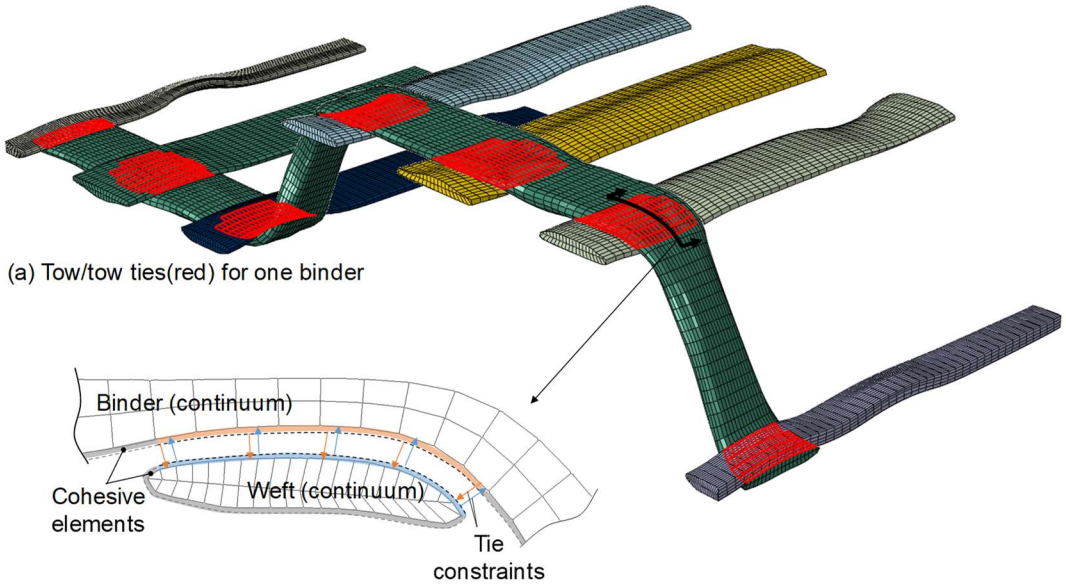

Figure 10. Tow/tow tie constraints for one binder tow.

and orange cohesive elements are those included in the tow/tow tie. The gray cohesive elements are tied to the matrix. A separate tie constraint is assigned for each group of cohesive elements (orange and blue) denoted by the orange and blue arrows. As with the tow/matrix interface, the cohesive element surface is the slave and the continuum element surface on the adjacent tow is the master in the tie constraint. Since the tow/tow interface has duplicate cohesive elements, the cohesive element strength and toughness properties are reduced by half. This duplicated cohesive element approach is used since with the misaligned meshes it is simpler to implement than automatically identifying and deleting the redundant cohesive elements.

Applying the described procedure to all of the tows and matrix results in 1040 tie constraints for the 3D woven example model. At this stage, the modeling specific to the fabric material is complete. Completing the rest of the model construction (specifying boundary conditions, defining material properties, etc.) follows generic PDA modeling procedures (e.g., [11]). Relevant details of the remaining model construction are summarized for the example loading scenario in the next section.

BEHAVIOR UNDER UNIAXIAL WARP TENSION

The features of the model are demonstrated with an example problem where the 3D woven model described thus far is loaded under warp-direction tension. The purpose of this exercise is to highlight qualitatively the progressive damage prediction capability of the model using test data available in the literature. It is emphasized that this example is a preliminary demonstration of the modeling approach and that further work is needed to fully exploit the capability.

Material properties

The material properties used in the analysis were obtained from data available in the literature. The matrix material is RTM-6 with elastic constants $E = 2890$ MPa and $v =$

0.35 [47]. Matrix plasticity is accounted for using an isotropic yield surface and tabular hardening response calibrated to match the tensile stress vs. strain curve reported in reference [48] for neat RTM-6 specimens tested under quasi-static loading rates. The tows are considered to be transversely isotropic having the elastic and strength properties given in Table 1 from reference [49] wherein these values are calculated based on the constituent AS4 and RTM-6 material properties. The fracture toughnesses for the matrix modes are $G_{Ic} = 0.216$ kJ/m^2 and $G_{IIc} = 0.857$ kJ/m^2 [50]. The tows are modeled with the CompDam material model considering fiber damage using conventional CDM and matrix cracking using the deformation gradient decomposition technique. The matrix strengths in Table 1 and fracture toughnesses noted above are also used for the tow/matrix and tow/tow interface debonding.

TABLE 1. Material properties for the AS4/RTM-6 tows [49].

E_1 (MPa)	E_2 (MPa)	G_{12} (MPa)	ν_{12}	ν_{23}	X_T (MPa)	Y_T (MPa)	S_L (MPa)
108590	10865	5765	0.23	0.25	2709	72	70

Analysis procedure

The analysis is conducted with an explicit dynamic procedure with a prescribed warp-direction extension specified by a smooth-step amplitude function through a duration of 0.1 sec. Automatic mass scaling is used with a target time increment size of 10^{-7} seconds. These simulation parameters were found to be sufficient to approximate quasi-static loading conditions, with almost no dynamic effects observed.

While the proposed model generation process could be adapted to allow for periodic boundary conditions, this has not been done here. Instead, the model is loaded in simple tension with the left and right (weft) faces being free. Since the modeled domain is small (only one unit cell), the edge effects from the free boundary conditions do influence the results. The author envisions the proposed modelling approach is most valuable when applied using a global/local modeling paradigm, as in [36, 14, 46]. Therefore, the simple boundary conditions used here are intended only for qualitative demonstration purposes.

The model contains about 870,000 elements and 3.9 million degrees of freedom. The analysis was conducted using double precision and was accelerated using domain-decomposition based parallelization across 80 Intel Skylake cores. The analysis took about 4 hours to complete.

Test procedure

The analysis results are compared with tests of specimens obtained from the plate designated ‘SN005’ in reference [34], the same plate from which the previously discussed X-Ray CT scans were obtained. The specimens were loaded monotonically and quasi-statically in uniaxial warp-direction tension by displacement control following ASTM D3039 [51] under ambient conditions. Nominal stress vs. strain was reported where the nominal stress is the load divided by the original cross-sectional area and the nominal strain was measured using digital image correlation between two points initially separated by 76 mm and centered on the gage section of the specimen. The reader is referred to reference [34] for complete details of the testing procedure.

Results and discussion

The results from the analysis are summarized in Figure 11. The nominal stress vs. strain from two test specimens and the analysis is shown in Figure 11a. From the onset of loading up to about 0.6% strain, there is excellent agreement between test and analysis, demonstrating that the model predicts the initial stiffness accurately. Beyond 0.6% strain, the analysis shows some nonlinearity whereas the test data is almost perfectly linear. At this time, it is unclear why the test results do not also exhibit some nonlinearity; further study is needed to resolve this discrepancy. The nonlinearity in the analysis results from the onset and propagation of matrix degradation modes including: 1) debonding between the binder tows and matrix starting where the binder tows turn through-the-thickness (light blue regions in Figure 11b), 2) matrix cracking in the weft tows, also near where the binder tows turn through-the-thickness (red regions in Figure 11b), and 3) plasticity in the matrix (not shown). From this, it is evident that the location where the binder tows turn from the surface to traversing the thickness is a critical location for damage onset. The same finding is reported for a different 3D orthogonal weave architecture in [18, 28] using detailed stress analysis. As these matrix degradation modes grow with increasing load, the nominal stress vs. strain curve becomes slightly more nonlinear up to about 1.25% where fiber fracture starts to occur. The warp tows fracture starting from the same critical location: where the binder tows turn through-the-thickness. The deformed warp and binder tows are shown in Figure 11c, with the elements that have experienced tensile fiber fracture hidden. Due to the architecture of the binder tows, the resulting fracture of the warp tows occurs on two distinct planes, as shown by the dashed black lines in Figure 11c, and are connected by a network of matrix cracks to produce two-piece failure. Once most of the warp tows fracture, the load drops. The agreement in terms of measured and predicted strength is observed to be quite good. The average measured strength was 773 MPa and the predicted strength is 714 MPa, for a percent error of -7.7%.

The warp-direction tension loading demonstration helps to illustrate the potential of the proposed modeling approach to provide a pathway toward reliable and predictive

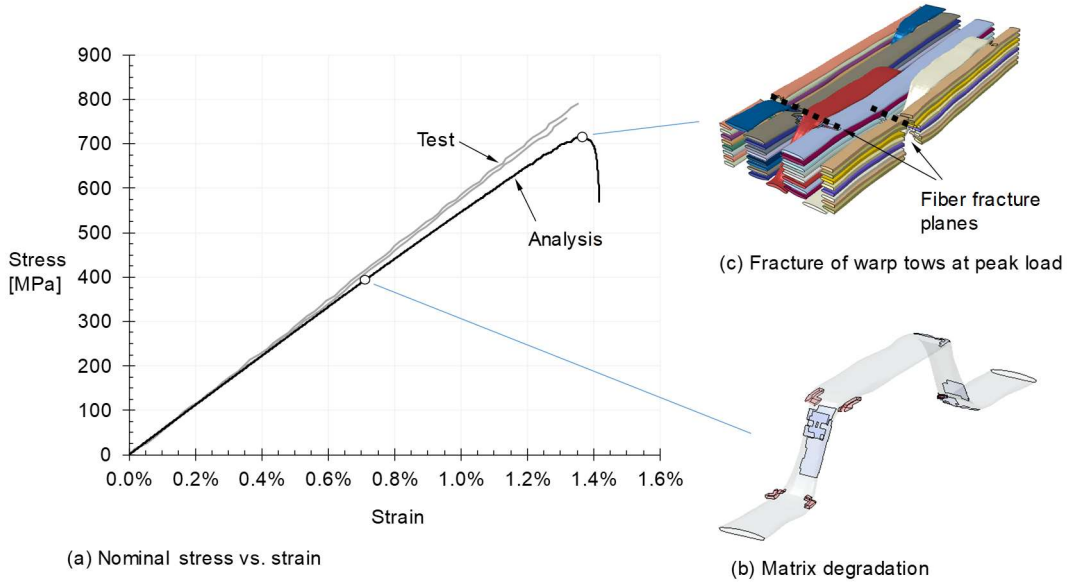

Figure 11. Test and analysis results for uniaxial warp-tension loading.

PDA for fabric composites. The results show that the model has the potential to predict the location and modes of different damage types including their onset, propagation, and interactions. While the results are promising, it is emphasized that further developments are required to mature the method including 1) establishing procedures for material property and as-manufactured weave characterization, 2) verification of the approach using simple closed-form or well understood problems, 3) demonstrating numerically the robustness and accuracy of the modeling approach for a variety of different fabrics, and 4) evaluating quantitatively the accuracy of the damage progression predictions under different loading scenarios.

SUMMARY

A new method was proposed for mesoscale progressive damage analysis of fabric composite structures. The proposed method builds on recent developments in damage analysis for composite structures made from laminated unidirectional plies, by introducing the same modeling procedures and best-practices where possible. The model construction process is agnostic to the fabric architecture, such that it can be applied to 2D fabrics and 3D fabrics in flat and formed (curved) configurations. The flexibility is afforded by a series of mesh-based operations to construct the tows and matrix solid meshes from an initial set of surface meshes of the tows. It is also noteworthy that the approach considers directly locations where tows touch as being connected with cohesive elements, thus avoiding the need to introduce arbitrary adjustments to the tow geometries.

The method was demonstrated for a particular 3D orthogonal weave. Since no geometry model existed for the particular weave architecture, a geometry model was created using the multi-chain digital element method, informed by several point measurements from an X-Ray computed tomography scan. The resulting geometry was shown to be in relatively good agreement with the as-manufactured state by overlaying the geometry model on top of X-Ray computed tomography scans at several locations in the volume. The geometry model was then used to create the finite element model using the proposed approach. The model was analyzed for uniaxial warp-direction loading and compared with test data for stiffness and strength. The results show that the model can predict the stiffness and strength accurately.

ACKNOWLEDGEMENTS

The author wishes to acknowledge the support of the NASA Composites Technology for Exploration project. Many thanks to Dr. David Mollenhauer (AFRL) for providing access to the VTMS software and guidance on its use. The tow material properties provided by Dr. Trent Ricks are also gratefully acknowledged.

REFERENCES

[1] F. Zhuang, A. Arteiro, C. Furtado, P. Chen, and P. P. Camanho, "Mesoscale modelling of damage in single- and double-shear composite bolted joints," Compos. Struct., vol. 226, p. 111210, Oct. 2019.

[2] Y. Xu, J. Jung, S. Nojavan, and Q. Yang, "An orthotropic augmented finite element method (A-FEM) for high-fidelity progressive damage analyses of laminated composites," Compos. Struct., vol. 229, p. 111416, Dec. 2019.

[3] S. Lin, S. I. Thorsson, and A. M. Waas, "Predicting the low velocity impact damage of a quasi-isotropic laminate using EST," Compos. Struct., p. 112530, Jun. 2020.

[4] J. Zhi and T.-E. Tay, "Interrogating failure mechanisms of notched composites through a discrete crack modeling approach," Compos. Sci. Technol., vol. 196, p. 108203, Aug. 2020.

[5] B. Y. Chen, S. T. Pinho, N. V. De Carvalho, P. M. Baiz, and T. E. Tay, "A floating node method for the modelling of discontinuities in composites," *Eng. Fract. Mech.*, vol. 127, pp. 104–134, Sep. 2014.

[6] N. V. De Carvalho, B. Y. Chen, S. T. Pinho, J. G. Ratcliffe, P. M. Baiz, and T. E. Tay, "Modeling delamination migration in cross-ply tape laminates," *Compos. Part Appl. Sci. Manuf.*, vol. 71, pp. 192–203, Apr. 2015.

[7] F. A. Leone Jr., C. G. Dávila, and D. Girolamo, "Progressive damage analysis as a design tool for composite bonded joints," *Compos. Part B Eng.*, vol. 77, pp. 474–483, Aug. 2015.

[8] F. A. Leone Jr., "Deformation gradient tensor decomposition for representing matrix cracks in fiber-reinforced materials," *Compos. Part Appl. Sci. Manuf.*, vol. 76, pp. 334–341, Sep. 2015.

[9] F. A. Leone Jr., C. G. Dávila, G. E. Mabson, M. Ramnath, and I. Hyder, "Fracture-based mesh size requirements for matrix cracks in continuum damage mechanics models," presented at the 58th AIAA/ASCE/AHS/ASC Structures, Structural Dynamics, and Materials Conference, AIAA SciTech Forum, Grapevine, TX, Jan. 2017.

[10] K. Song, F. A. Leone Jr., and C. A. Rose, "Continuum damage mechanics models for the analysis of progressive damage in cross-ply and quasi-isotropic panels subjected to static indentation," presented at the 59th AIAA/ASCE/AHS/ASC Structures, Structural Dynamics, and Materials Conference, AIAA SciTech Forum, Kissimmee, FL, Jan. 2018.

[11] F. A. Leone Jr., K. Song, W. M. Johnston, C. A. Rose, W. C. Jackson, and C. G. Dávila, "Test/analysis correlation of damage states in stiffened post-buckled validation building block specimens," presented at the 34th American Society for Composites Technical Conference, Atlanta, GA, Sep. 2019.

[12] H. K. Adluru, K. H. Hoos, E. V. Iarve, and J. G. Ratcliffe, "Delamination initiation and migration modeling in clamped tapered laminated beam specimens under static loading," *Compos. Part Appl. Sci. Manuf.*, vol. 118, pp. 202–212, Mar. 2019.

[13] N. V. De Carvalho, G. E. Mabson, R. Krueger, and L. R. Deobald, "A new approach to model delamination growth in fatigue using the Virtual Crack Closure Technique without re-meshing," *Eng. Fract. Mech.*, vol. 222, p. 106614, Dec. 2019.

[14] F. A. Leone Jr., K. Song, C. Rose, and W. Jackson, "Progressive damage analysis of post-buckled stiffened panels under static compressive loading," presented at the 61st AIAA/ASCE/AHS/ASC Structures, Structural Dynamics, and Materials Conference, AIAA SciTech Forum, Orlando, FL, Jan. 2020.

[15] B. N. Cox, W. C. Carter, and N. A. Fleck, "A binary model of textile composites—I. Formulation," *Acta Metall. Mater.*, vol. 42, no. 10, pp. 3463–3479, Oct. 1994.

[16] N. Isart, B. El Said, D. S. Ivanov, S. R. Hallett, J. A. Mayugo, and N. Blanco, "Internal geometric modelling of 3D woven composites: A comparison between different approaches," *Compos. Struct.*, vol. 132, pp. 1219–1230, Nov. 2015.

[17] A. Ewert, B. Drach, K. Vasylevskyi, and I. Tsukrov, "Predicting the overall response of an orthogonal 3D woven composite using simulated and tomography-derived geometry," *Compos. Struct.*, vol. 243, p. 112169, Jul. 2020.

[18] M. K. Ballard and J. D. Whitcomb, "Stress analysis of 3D textile composites using high performance computing: new insights and challenges," *IOP Conf. Ser. Mater. Sci. Eng.*, vol. 406, p. 012004, Sep. 2018.

[19] Y. Wang and X. Sun, "Digital-element simulation of textile processes," *Compos. Sci. Technol.*, vol. 61, no. 2, pp. 311–319, Feb. 2001.

[20] G. Zhou, X. Sun, and Y. Wang, "Multi-chain digital element analysis in textile mechanics," *Compos. Sci. Technol.*, vol. 64, no. 2, pp. 239–244, Feb. 2004.

[21] E. Zhou, D. Mollenhauer, and E. Iarve, "Micro-Geometric Modeling of Textile Preforms with Vacuum Bag Compression: An Application of Multi-chain Digital Element Technique," presented at the 49th AIAA/ASME/ASCE/AHS/ASC Structures, Structural Dynamics, and Materials Conference, Schaumburg, IL, Apr. 2008.

[22] R. G. Rinaldi, M. Blacklock, H. Bale, M. R. Begley, and B. N. Cox, "Generating virtual textile composite specimens using statistical data from micro-computed tomography: 3D tow representations," *J. Mech. Phys. Solids*, vol. 60, no. 8, pp. 1561–1581, Aug. 2012.

[23] X. Liu *et al.*, "Refine reconstruction and verification of meso-scale modeling of three-dimensional five-directional braided composites from X-ray computed tomography data," *Compos. Struct.*, vol. 245, p. 112347, Aug. 2020.

[24] S.-Y. Hsu and R.-B. Cheng, "Modeling geometry and progressive interfacial damage in textile composites," *J. Compos. Mater.*, vol. 47, no. 11, pp. 1343–1356, May 2013.

[25] T. Wehrkamp-Richter, N. V. De Carvalho, and S. T. Pinho, "A meso-scale simulation framework for predicting the mechanical response of triaxial braided composites," *Compos. Part Appl. Sci. Manuf.*, vol. 107, pp. 489–506, Apr. 2018.

[26] T. Wehrkamp-Richter, N. V. De Carvalho, and S. T. Pinho, "Predicting the non-linear mechanical response of triaxial braided composites," *Compos. Part Appl. Sci. Manuf.*, vol. 114, pp. 117–135, Nov. 2018.

[27] Y. Hu, Q. Zhou, X. Gao, A. Jacobsen, D. Zorin, and D. Panozzo, "Tetrahedral meshing in the wild," *ACM Trans Graph*, vol. 37, no. 4, Aug. 2018.

[28] M. K. Ballard and J. D. Whitcomb, "Detailed stress analysis of a twill orthogonally woven textile composite," *J. Compos. Mater.*, p. 0021998320920920, Apr. 2020.

[29] S. Yan, X. Zeng, and A. Long, "Meso-scale modelling of 3D woven composite T-joints with weave variations," *Compos. Sci. Technol.*, vol. 171, pp. 171–179, Feb. 2019.

[30] E. V. Iarve, D. H. Mollenhauer, E. G. Zhou, T. Breitzman, and T. J. Whitney, "Independent mesh method-based prediction of local and volume average fields in textile composites," *Compos. Part Appl. Sci. Manuf.*, vol. 40, no. 12, pp. 1880–1890, Dec. 2009.

[31] A. Mazumder, Y. Wang, and C.-F. Yen, "A structured method to generate conformal FE mesh for realistic textile composite micro-geometry," *Compos. Struct.*, vol. 239, p. 112032, May 2020.

[32] F. A. Leone Jr., A. C. Bergan, and C. G. Dávila, *CompDam - Deformation Gradient Decomposition (DGD)*. 2020. https://github.com/nasa/CompDam_DGD

[33] E. Zhou and D. Mollenhauer, "Introduction to VTMS, version 3.0," 88ABW-2017–2554, 2017.

[34] B. Farrokh, K. Segal, T. Ricks, S. G. Miller, B. T. Rodini, and D. W. Sleight, "Uniaxial tensile properties of AS4 3D woven composites with four different resin systems: experimental results and analysis- property computations," presented at The Composites and Advanced Materials Expo (CAMX), Anaheim, CA, Sep. 2019.

[35] I. M. Gitman, H. Askes, and L. J. Sluys, "Representative volume: Existence and size determination," *Eng. Fract. Mech.*, vol. 74, no. 16, pp. 2518–2534, Nov. 2007.

[36] W. M. van der Brink, G. van de Vrie, and M. Nawijn, "Modelling and simulation of damage in woven fabric composites on meso-macro level using the independent mesh method," National Aerospace Laboratory NLR, NLR-TP-2012-129, Nov. 2013.

[37] A. Drach, B. Drach, and I. Tsukrov, "Processing of fiber architecture data for finite element modeling of 3D woven composites," *Adv. Eng. Softw.*, vol. 72, pp. 18–27, Jun. 2014.

[38] Dawson-Haggerty et al., *trimesh*. 2019. https://trimsh.org/

[39] S. van der Walt, S. C. Colbert, and G. Varoquaux, "The NumPy array: A structure for efficient numerical computation," *Comput. Sci. Eng.*, vol. 13, no. 2, pp. 22–30, Mar. 2011.

[40] P. Cignoni, M. Callieri, M. Corsini, M. Dellepiane, F. Ganovelli, and G. Ranzuglia, "MeshLab: An open-source mesh processing tool," in *Eurographics Italian Chapter Conference*, 2008.

[41] Y. Hu, T. Schneider, B. Wang, D. Zorin, and D. Panozzo, "Fast tetrahedral meshing in the wild," arXiv:1908.03581v2 [cs.GR], 2020.

[42] G. Barill, N. Dickson, R. Schmidt, D. I. W. Levin, and A. Jacobson, "Fast winding numbers for soups and clouds," *ACM Trans. Graph.*, vol. 37, no. 4, 2018.

[43] Zhou, Q. et al., *PyMesh*. 2019. https://pymesh.readthedocs.io/en/latest/

[44] Q. Zhou, E. Grinspun, D. Zorin, and A. Jacobson, "Mesh arrangements for solid geometry," *ACM Trans. Graph. TOG*, vol. 35, no. 4, pp. 39:1–39:15, Jul. 2016.

[45] *ABAQUS Online Documentation: Version 2019*. Providence, RI: Dassault Systèmes Simulia Corporation, 2019.

[46] J. Action, F. A. Leone, and N. V. D. Carvalho, "Progressive damage analysis of a multi-stringer post-buckled panel," in *AIAA Scitech 2020 Forum*, Jan. 2020, doi: 10.2514/6.2020-1481.

[47] C. Brauner, S. Bauer, and A. S. Herrmann, "Analysing process-induced deformation and stresses using a simulated manufacturing process for composite multispar flaps," *J. Compos. Mater.*, Feb. 2014.

[48] R. Gerlach, C. R. Siviour, N. Petrinic, and J. Wiegand, "Experimental characterisation and constitutive modelling of RTM-6 resin under impact loading," *Polymer*, vol. 49, no. 11, pp. 2728–2737, May 2008.

[49] T. M. Ricks, E. J. Pineda, B. A. Bednarcyk, and S. M. Arnold, "Application of the NASA multiscale analysis tool: Multiscale integration and interoperability," presented at The Conference on Advancing Analysis & Simulation Engineering, Jun. 16, 2020.

[50] Z. Wu, X.-S. Yi, and A. Wilkinson, "Interlaminar fracture toughness of carbon fibre/RTM6-2 composites toughened with thermoplastic-coated fabric reinforcement," *Compos. Part B Eng.*, vol. 130, pp. 192–199, Dec. 2017.

[51] ASTM Standard D3039. "Standard Test Method for Tensile Properties of Polymer Matrix Composite Materials," in *Annual Book of ASTM Standards*, vol. 15.03, W. Conshohocken, PA: ASTM Int., 2007.